Plasma Chemistry and Plasma Processing, Vol. 24, No. 4, December 2004 (© 2004)

In-Flight Spheroidization of Alumina Powders in Ar–H_2 and Ar–N_2 Induction Plasmas

R. Ye,[1,2] T. Ishigaki,[2,3] J. Jurewicz,[1] P. Proulx,[1] and M. I. Boulos[1]

Received July 31, 2003; revised February 3, 2004

In-flight spheroidization of alumina powders in Ar–H_2 (H_2–7.6%, vol/vol) and Ar–N_2 (N_2–13.0%, vol/vol) RF induction plasmas was investigated numerically and experimentally. The mathematical model for the plasma flows incorporates the k–ε turbulence model, and that for particles is the Particle-Source-in-Cell (PSI-Cell) model. Experimental results demonstrate that spheroidized alumina particles are produced in both Ar–H_2 and Ar–N_2 RF plasmas, with different particle size distributions and crystal phases. Agreement between the predicted and measured particle size distributions is satisfactory under high particle feed rate conditions, while the results obtained for the Ar–H_2 plasma are better than those for the Ar–N_2 plasma. The discrepancy occurring in low feed rate conditions suggests that particle evaporation is an important factor affecting the plasma–particle heat transfer.

KEY WORDS: RF plasma; particle spheroidization; size distribution; gas mixture.

1. INTRODUCTION

RF induction plasmas have been widely applied to materials processing such as spheroidization of ceramic powders and deposition of the various coatings.[1,2] In-flight particles are heated in the high temperature region of the plasma and eventually melted during the treatment. In the particle spheroidization process, the molten particles are spheroidized by rapidly cooling of particles from the liquid phase. The crystal phase of a particle is determined by its temperature history. The heating efficiency depends strongly on the particle properties and powder feeding conditions, as well as the operating conditions of the plasma generator.[3]

[1]Department of Chemical Engineering, University of Sherbrooke, Sherbrooke, Quebec, Canada J1K 2R1.
[2]National Institute for Materials Science, Advanced Materials Laboratory, 1-1 Namiki, Tsukuba, Ibaraki 305-0044, Japan.
[3]To whom correspondence should be addressed. Telephone: 81-29-860-4659; fax: 81-29-860-4701; e-mail: ishigaki.takamasa@nims.go.jp

0272-4324/04/1200-0555/0

A preliminarily study on alumina (Al_2O_3) powder spheroidization in RF plasmas has been carried out by Ishigaki and Boulos.[4] In a subsequent research, Ishigaki *et al.* investigated the deposition of spheroidized alumina particles from both the vapor and the molten particle phases in RF plasmas.[5] It was demonstrated that the growth form of the deposits produced from the vapor phase varied with the plasma-generating and powder-feeding conditions. Two mixtures of plasma gases, Ar–H_2 and Ar–N_2, were used in the experiments to examine their respective effects on the evaporation and spheroidization of alumina powders. It was found that the heat transfer rate between the plasma and the particles in the Ar–H_2 plasma is higher than that in the Ar–N_2 plasma.

Both experimental and numerical investigations are important in the research and development of the thermal plasma technologies. In plasma processing of particulate materials, the experimental results usually present information on the final characteristics of the particles. Alternatively, mathematical modeling provides insight on the thermal histories of the in-flight particles during the plasma processing. The objective of this study is to investigate the particle spheroidization in RF plasmas, with emphasis on the effects of gas composition on the plasma–particle heat transfer. Mathematical modeling of particle heating in Ar–H_2 and Ar–N_2 RF plasmas was conducted under turbulent plasma flow conditions. The predicted results, mainly particle size distributions after plasma treatment, are compared with the test results obtained under the corresponding experimental conditions. This leads to better understanding of the powder treatment process in the RF plasmas, and consequently is helpful to optimize the operating conditions in plasma processing of particulate materials.

2. THE EXPERIMENTAL SET-UP

Figure 1 schematically shows the RF plasma treatment system used in the spheroidization of alumina particles. It includes an RF plasma torch, a reaction chamber, and powder collection units. The RF plasma torch is the Tekna PL-50 model, 170 mm in length and 50 mm in ID, with a water-cooled quartz wall. The induction coil has five turns and the RF frequency is 3 MHz. Alumina powders premixed with carrier gas are injected into the plasma reactor through the central probe (90 mm) inserted into the high temperature region of the plasma torch. Detailed configuration of this RF plasma torch were shown by Chen.[6] Two kinds of working gases: Ar–H_2 (H_2–7.6%, vol/vol) and Ar–N_2 (N_2–13.0%, vol/vol), were utilized in the study to reveal the effects of working gas on the heating and spheroidization of alumina powders. The water-cooled reaction chamber is made of stainless steel with a diameter of 254 mm. The exhaust gases from the

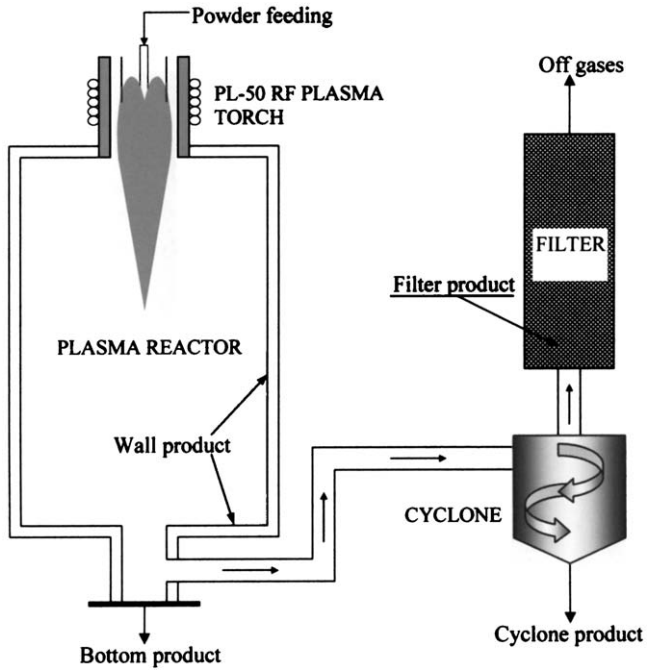

Fig. 1. Schematic of the RF plasma reactor used for alumina powder spheroidization.

chamber are treated through a cyclone and filters to separate the fine particles from the gases. The dimensions for the RF plasma reactor and the operating conditions in the present study are listed in Table I.

Alumina powders with a mean diameter of 24.5 μm and a standard deviation of 6.0 μm were used in the experiments. The original particle crystal phase was α-phase. After treatment, the alumina powders were collected from four different places: the chamber wall, the bottom of the chamber, the cyclone and the filters. The products were analyzed using sedigraphy, scanning electron microscope (SEM) and X-ray diffractometry, in order to obtain information on the particle size distributions, the particle shapes, the surface morphologies, and the crystal phases of the particles.

3. THE MATHEMATICAL MODELS

3.1. The Models

The mathematical models include two parts: conservation equations for the RF plasma and the k–ε turbulence model, and the Particle-Source-In-Cell (PSI-Cell) model[7] for the particles.

Table I. Dimensions for RF Plasma Reactor and Operating Conditions

Inner radius of central tube (R_1)	2.0 mm	Length of plasma reactor (L_T)	1020.0 mm
Outer radius of central tube (R_2)	4.5 mm	Thickness of wall (d_w)	3.5 mm
Radius of sheath tube (R_3)	21.0 mm	Number of RF coil (N_c)	5 turn
Inner radius of plasma torch (R_0)	25.0 mm		
Radius of RF coil (R_c)	33.0 mm	Plate power (P)	40 kW
Radius of reactor (R_T)	127.0 mm	Chamber pressure (p)	400 Torr
Position of first RF coil (L_1)	60.0 mm	RF frequency (f)	3 MHz
Position of last RF coil (L_2)	120.0 mm	Flow rate of carrier gas (Q_1)	6.9 slpm (Ar/N_2)
Length of plasma torch (L_3)	170.0 mm	Flow rate of plasma gas (Q_2)	28.0 slpm (Ar)
Length of central tube (L_p)	90.0 mm	Flow rate of sheath gas (Q_3)	82.0 slpm (Ar)+
Length of sheath tube (L_s)	50.0 mm		9.6 slpm(H_2/N_2)

The plasma model is based on the assumptions that the plasma is a steady-state turbulent flow in axisymmetric cylindrical geometry, it is in local thermodynamic equilibrium (LTE) and optically thin, and there is negligible viscous dissipation. Based on the foregoing assumptions, the two-dimensional conservation equations for the mass, the momentum (u, v, w), the energy (h), and those for the turbulent kinetic energy (k) and its dissipation rate (ε), are given. Those equations may be written into a general form as follows:

$$\frac{\partial}{\partial z}(\rho u\phi) + \frac{1}{r}\frac{\partial}{\partial r}(r\rho v\phi) = \frac{\partial}{\partial z}\left(\Gamma_\phi \frac{\partial \phi}{\partial z}\right) + \frac{1}{r}\frac{\partial}{\partial r}\left(r\Gamma_\phi \frac{\partial \phi}{\partial r}\right) + S_\phi + S_\phi^{\mathrm{p}}, \quad (1)$$

where ρ, u, v are the plasma density, axial and radial velocity components, respectively. ϕ, Γ_ϕ are a dependent variable and its diffusion coefficient. The diffusion coefficient consists of molecular and turbulent transport properties. S_ϕ and S_ϕ^{p} are the corresponding source terms contributed by the plasma and particles. The dependent variables, transport coefficients, and source terms for the conservation equations are listed in Table II. In the table, μ_{m} and μ_{t} are the respective molecular and turbulent viscosities, λ is the thermal conductivity and C_{p} is the specific heat at constant pressure, Pr_{t} is the turbulent Prandtl number, Sc_{m} and Sc_{t} are the molecular and turbulent Schmidt numbers, respectively. σ_k, σ_ε, C_μ, C_1, C_2 are constants for the k–ε turbulence model. F_{z} and F_{r} are the corresponding axial and radial components of Lorentz force, P_0 and R are the volumetric Joule heating and the radiation loss rates, respectively. A detailed

Table II. Dependent Variables, Coefficients and Source terms for the Conservation Equations

ϕ	Γ_ϕ	S_ϕ	S_ϕ^{p}
1	0	0	S_m^{p}
u	μ_e	$-\frac{\partial p}{\partial z}+\frac{\partial}{\partial z}\left(\mu_e\frac{\partial u}{\partial z}\right)+\frac{1}{r}\frac{\partial}{\partial r}\left(r\mu_e\frac{\partial v}{\partial z}\right)+F_z$	S_u^{p}
v	μ_e	$-\frac{\partial p}{\partial z}+\frac{\partial}{\partial z}\left(\mu_e\frac{\partial u}{\partial r}\right)+\frac{1}{r}\frac{\partial}{\partial r}\left(r\mu_e\frac{\partial v}{\partial r}\right)-\frac{2\mu_e v}{r^2}+\frac{\rho w^2}{r}+F_r$	S_v^{p}
w	μ_e	$-\frac{w}{r}\left(\rho v+\frac{\mu_e}{r}+\frac{\partial\mu_e}{\partial r}\right)$	S_w^{p}
h	$\lambda/C_{\mathrm{p}}+\mu_{\mathrm{t}}/Pr_{\mathrm{t}}$	P_0-R	S_E^{p}
y	$\mu_m/Sc_{\mathrm{m}}+\mu_{\mathrm{t}}/Sc_{\mathrm{t}}$	0	0
k	$\mu_{\mathrm{m}}+\mu_{\mathrm{t}}/\sigma_{\mathrm{k}}$	$G-\rho\varepsilon^*$	0
ε	$\mu_{\mathrm{m}}+\mu_{\mathrm{t}}/\sigma_\varepsilon$	$\frac{\varepsilon}{k}(C_1G-C_2\rho\varepsilon)$	0

$\mu_e=\mu_{\mathrm{m}}+\mu_{\mathrm{t}},\ \mu_{\mathrm{t}}=\rho C_\mu k^2/\varepsilon,\ Pr_{\mathrm{t}}=0.7,\ Sc_{\mathrm{m}}=0.7,\ Sc_{\mathrm{t}}=1.0,\ \sigma_k=1.0,$
$\sigma_\varepsilon=1.3,\ C_\mu=0.09,\ C_1=1.44,\ C_2=1.92$

$^*G=\mu_{\mathrm{t}}\left\{2\left[\left(\frac{\partial u}{\partial z}\right)^2+\left(\frac{\partial v}{\partial r}\right)^2+\left(\frac{v}{r}\right)^2\right]+\left(\frac{\partial w}{\partial r}-\frac{w}{r}\right)^2+\left(\frac{\partial w}{\partial z}\right)^2+\left(\frac{\partial v}{\partial r}+\frac{\partial u}{\partial r}\right)^2\right\}$

description of the plasma model and the k–ε turbulence model may be found in Refs. 6 and 8.

The particle model is based on the assumptions that a particle is spherical in shape with infinite internal thermal conductivity. The effect of particle vapor on the plasma transport properties is not considered, but the contribution of particle vapor to the continuity equation is included. The interactions between particles are also neglected. It should be pointed out that some effects neglected in the model could have influence on the particle dynamics and heat transfer in the thermal plasma. For example, the drag coefficient of a particle may be affected by the shape of a particle. It increases with the decrease of sphericity, which is defined as the ratio of the surface area of a sphere having the same volume to the surface area of the particle. Extensive reviews of the various effects on particle dynamics and heat transfer are found in Refs. 9 and 10. The influence of plasma turbulence on the particle dynamics, which leads to particle turbulent dispersion, is included. It is found that the dynamics of an alumina particle with diameter of 45 μm is affected by the particle turbulent dispersion.[11] Therefore, the plasma–particle heat transfer should be influenced by the turbulent dispersion due to the change of particle trajectory and residence time in the plasma. The exchange rates of heat and momentum between the plasma and particles, shown as source terms in the governing equations for the plasma and particles, are taken into account through the PSI-Cell model. The particle trajectory is obtained by integrating the equations of motion for the particle. The particle temperature is determined by the energy balance on the particle surface, which includes the energies for particle heating and evaporation, convective heat transfer and radiative energy loss. Mass, heat and momentum transfer rates between the plasma and the

particles are calculated simultaneously in the integration procedures. One can refer to Refs. 11 and 12 to find details on the particle model that is used in the present work.

3.2. The Boundary and Initial Conditions

The boundary conditions for the plasma flow and the electromagnetic field are the same ones described by Chen.[6] The initial conditions for the particle velocity and temperature are set to be equal to that of the carrier gas, e.g., the particles have a uniform velocity profile at the starting point (the tip of the probe) with initial temperature of 300 K. The walls are impermeable to particles, so the particles rebound into the plasma as they reach the walls.

3.3. The Solution Method

The computations were performed based on the plasma reactor shown in Fig. 1. The governing equations for the plasma were solved in a 77×85 non-uniform grid system for the calculation domain using the SIMPLER algorithm.[13] The thermodynamic and transport properties for pure gases were taken from the tabulated data of Boulos *et al.*[14] For gas mixture, the viscosity and thermal conductivity were calculated using the Wilke's formula,[15] and other properties were obtained using mass-fraction-weighted average. The effects of pressure on the transport and thermodynamic properties were considered by using the relations given in Ref. 6. An illustrative plot of the thermal conductivities of pure Ar, H_2, N_2, and the mixtures Ar–H_2 and Ar–N_2 used in the study, at 400 Torr, is shown in Fig. 2.

In modeling the particles, the required particle number, representing particle size distribution, injection point, and turbulence history, was tested until statistically stable solutions had been reached in each case. In the present study, the alumina particles are assumed to have 41 different sizes, each particle is injected into the plasma at 12 evenly spaced radial positions in the central tube, and this is repeated four times, which corresponds to four different turbulent dispersion histories. The combination of each probability for particle size, injection position and turbulent dispersion history yields a total number of 1968 trajectories.

4. RESULTS AND DISCUSSION

4.1. Temperature and Velocity Fields in the Ar–H_2 and Ar–N_2 RF Plasmas

The predicted plasma temperature and the axial velocity fields, at plate power of 40 kW (equivalent to 28 kW deposited power in plasma)

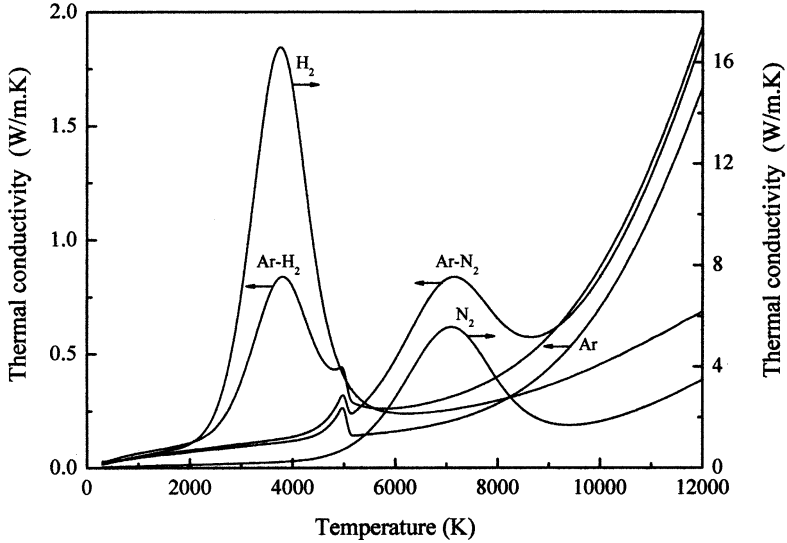

Fig. 2. Thermal conductivities of Ar, H_2, N_2, 92.4% Ar + 7.6% H_2 (vol/vol), and 87.0% Ar + 13.0% N_2 (vol/vol) at 400 Torr.

and chamber pressure of 400 Torr, are illustrated in Fig. 3(a) and (b), respectively.

The average Reynolds number at the inlet of the torch is 2810 for the Ar–H_2 plasma, and is 2746 for the Ar–N_2 plasma. The results for the Ar–H_2 plasma are shown on the left-hand side of each figure, with the corresponding results for Ar–N_2 plasma on the other side. It may be noticed that in the upstream region of the flow ($z < 300$ mm), the temperature of Ar–H_2 plasma is much higher than that of the Ar–N_2 plasma. However, the high temperature region of Ar–H_2 plasma shrinks much faster than that of the Ar–N_2 plasma. These lead to a broader Ar–H_2 plasma, but a longer Ar–N_2 plasma. These phenomena are mainly due to the different thermophysical properties of H_2 and N_2. For instance, as shown in Fig. 2, the Ar–H_2 plasma has much higher thermal conductivity between 3000 and 5000 K, which causes significant energy losses on the fringes of the plasma and results in a shorter plasma plume. Similar phenomena have also been reported by Girshick and Yu[16] in their observations and simulations for different RF plasmas.

4.2. Particle Size Distributions

Figure 4 indicates the particle size histories depend greatly on particle size. A small particle, of diameter $d_p = 6.5\,\mu$m, is seen to be fully

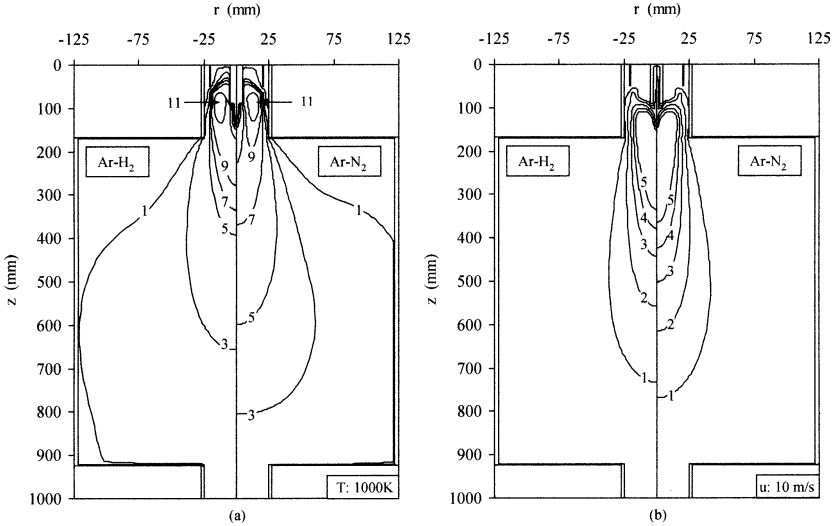

Fig. 3. (a) Temperature and (b) axial velocity fields for Ar–H_2 and Ar–N_2 RF plasmas, 40 kW, 400 Torr.

evaporated after it travels around 300 mm in the Ar–H_2 plasma. A larger particle, with $d_p = 42.5\,\mu$m, does not experience any evaporation at all. All particle evaporation occurs in a range from $z = 160$ to 380 mm in the Ar–H_2 plasma. Figure 4(b) shows that the smaller particles are evaporated more readily in the Ar–N_2 plasma. Even a particle of diameter 15.5 μm becomes fully evaporated in this case, revealing a higher total plasma–particle heat transfer during the heating history in the Ar–N_2 plasma than that in the Ar–H_2 plasma.

The predicted particle size distributions are compared with the corresponding measured values. In the experiments, most of the powders were collected on the chamber walls. The particle size distributions were obtained using sedigraphy. Figure 5(a) and (b) illustrate the predicted and measured particle size distributions in different plasmas and under different particle-feeding conditions. It is found in Fig. 5(a) that the particle size distributions shift to the left-hand side of the figure when the particle feed rate is decreased. This shift clearly indicates that particle evaporation occurs during the particle spheroidization process. Generally, the predicted results are found to be in fairly good agreement with the experiments. It is noticed that the predicted particle sizes are always smaller than those collected in the experiments. This tendency may be attributed to the presence of some spongy masses surrounding the larger particles. The agglomeration of such spongy masses on a particle, if present, interferes with

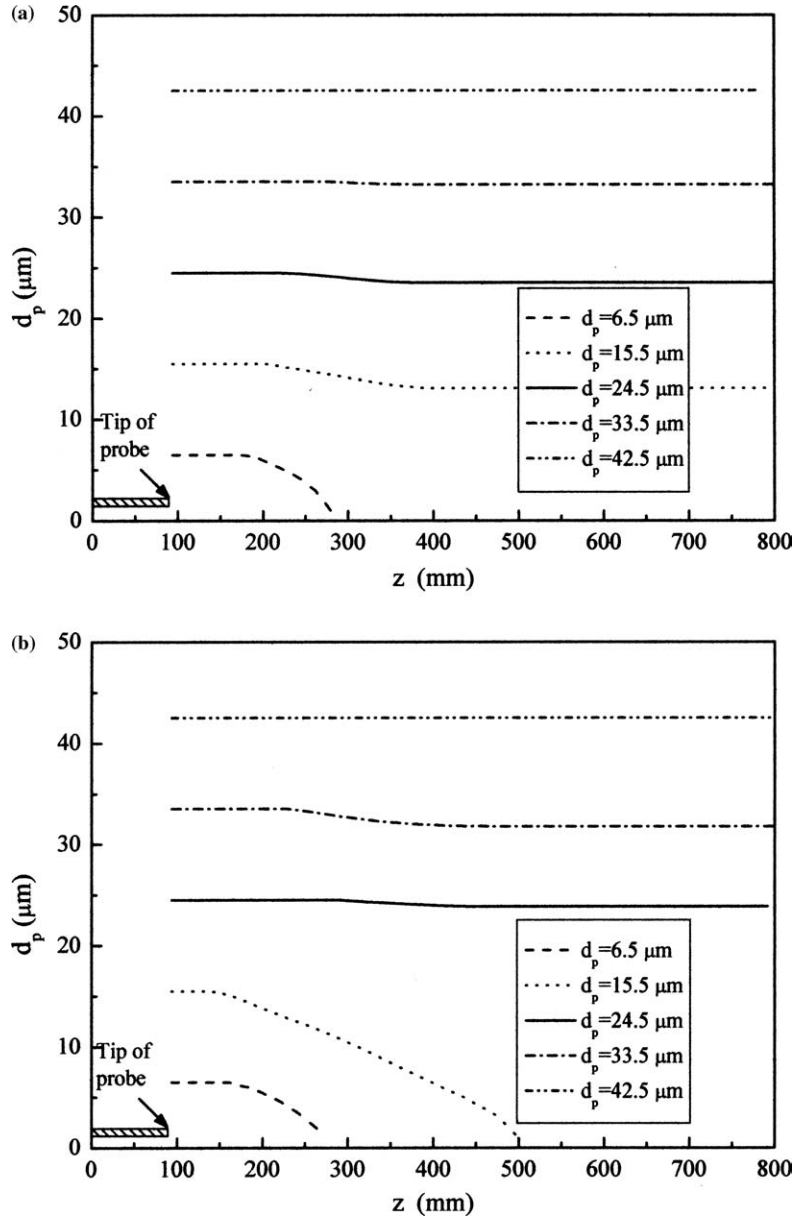

Fig. 4. Al_2O_3 particle diameter histories in (a) Ar–H_2 and (b) Ar–N_2 plasmas. Mean particle size 24.5 μm.

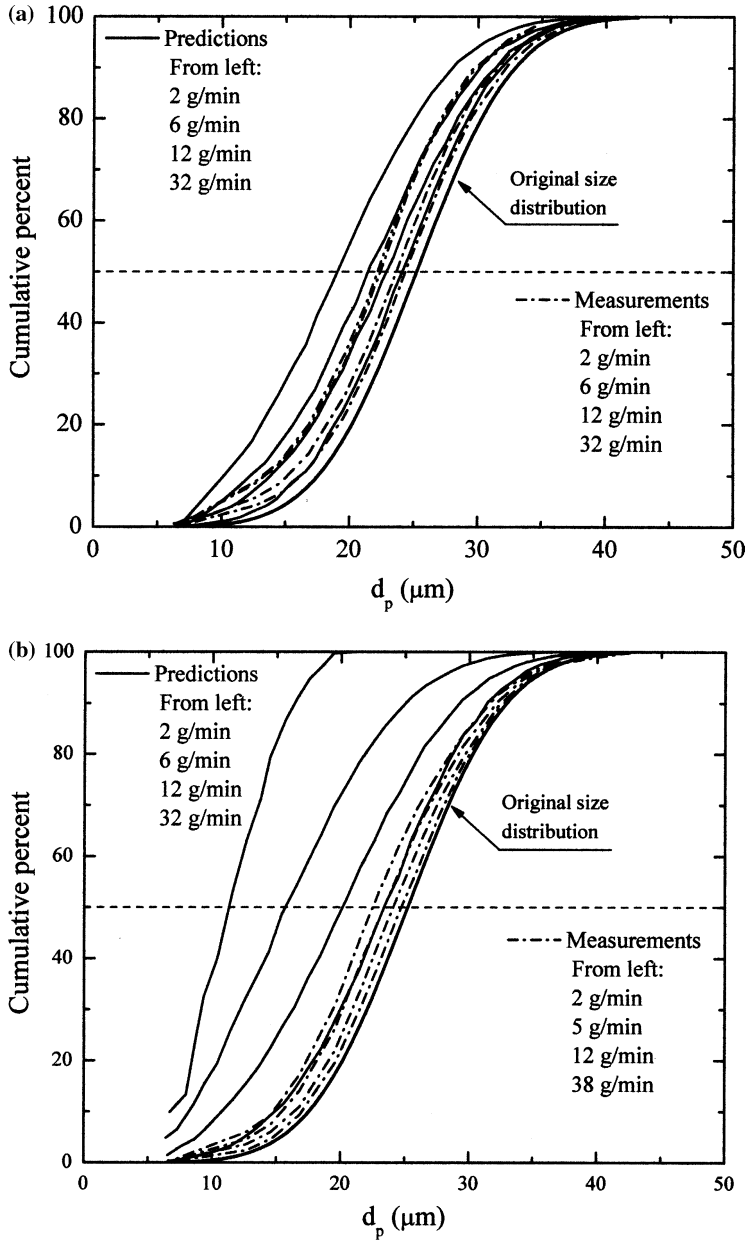

Fig. 5. The predicted particle size distributions and the corresponding measurements of Al_2O_3 treated in (a) Ar–H_2 and (b) Ar–N_2 plasmas.

the correct size measurement, leading to an overestimation of the particle diameter. It could be observed on the SEM images shown later that the condensation of vaporized powder into a spongy mass has a particularly strong influence for low feed rates in the $Ar–H_2$ plasma. Therefore, the experimental data should be shifted to the left.

The greater deviation of predictions from the measurements under lower feed rate conditions may be attributed to some effects of particle vapor which are not taken into account in the model. When a particle is evaporating, the vapor cloud forms and extends from the particle surface to 3–5 times its original radii. The mass flux of the vapor from an evaporating particle to the surrounding plasma reduces the heat flux to the particle by convective heat transfer which is in the opposite direction of the heat flux from the plasma to the particle. This effect becomes particularly pronounced at lower particle feed rates under which conditions the particles are easier to be evaporated. Moreover, the vapor surrounding an evaporating particle not only absorbs the thermal energy, but also modifies the transport properties of the medium around the particle.[17,18] Neglecting these effects results in an overestimation of the plasma–particle heat transfer, which has significant influence on predicting particle sizes in the presence of particle evaporation.

The variations in the values of d_{50}, the diameter of the 50% cumulative particle masses, with the feed rate, are shown in Fig. 6(a) and (b) for the $Ar–H_2$ and $Ar–N_2$ plasmas, respectively. These results again demonstrate that the predicted and experimental data match each other very well under high feeding conditions, but the differences become larger as the feed rate decreases. The predicted d_{50} sizes are always smaller than the experimental ones. It is also found that the predicted particle sizes are much smaller than those obtained in the experiments under the low feed rate conditions in the $Ar–N_2$ plasma. These observations reveal that the predicted heat transfer rate between the $Ar–N_2$ plasma and the particles is much higher than the real one.

Under both working gas conditions, the predictions made for $Ar–H_2$ plasma provide a better fit to the experimental observations than those for the $Ar–N_2$ plasma. The measured particle sizes of the $Ar–H_2$ plasma treated powders are smaller than those of the $Ar–N_2$ plasma treatment, which can be interpreted to mean that the heat transfer rate in the $Ar–H_2$ plasma is greater. However, the predictions of the model have an opposite trend under low feed rate conditions.

This phenomenon could be due to the treatment of the thermophysical and transport properties of the mixed-gas plasma. These properties were calculated according to the concentration of each gas component in the plasma. Diffusion in the mixed-gas plasmas depends on gradients in

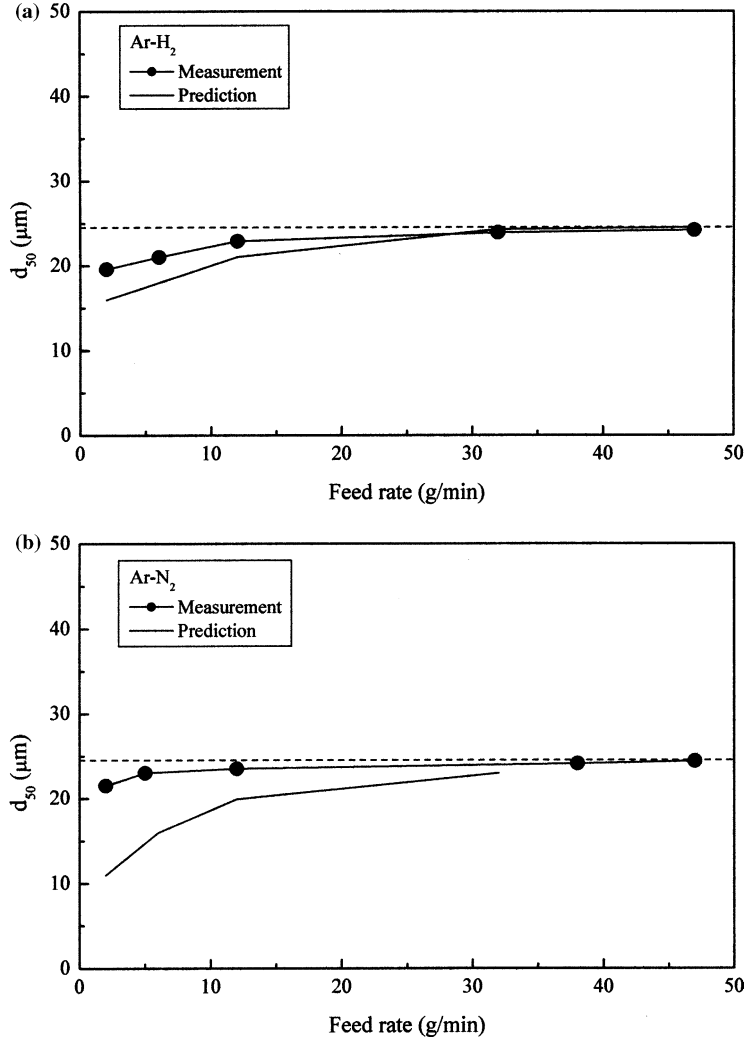

Fig. 6. The diameters of 50% cumulative particle mass of Al_2O_3 powders treated in (a) Ar–H_2 and (b) Ar–N_2 plasmas.

composition, temperature and pressure, and the applied electrical field, as well as ambipolar diffusion.[19] The diffusion coefficient was simplified in the present model, and it may therefore have resulted in errors arising in the prediction of concentration fields of the gases, and consequently the thermodynamical and transport properties of the plasma. Some other effects, such as demixing, may also affect the transport properties in the

plasma, and eventually influence the plasma–particle heat transfer. For example, the demixing in an Ar–H_2 plasma leads to a high concentration of hydrogen in the high temperature regions, which increases the thermal conductivity in these regions.[20]

4.3. Particle Shape and Crystal Phase

Figure 7 shows SEM photographs of the initial and the Ar–N_2 plasma treated alumina powders. The initial powders seen in Fig. 7(a) are typical of those used for spray coating applications and show irregularity in particle shapes. Figure 7(b) demonstrates that spheroidization is accomplished at the feed rate of 11 g/min, indicating sufficient melting of the particles in the plasma. The powder surfaces are relatively clean, even at the feed rate of 2 g/min, indicating that little agglomeration of particle vapor has occurred, see Fig. 7(c). In Fig. 8(a)–(c), photographs for the Ar–H_2 plasma treated particles are shown. At the higher particle feed rate (47 g/min), shown in Fig. 8(a), some particles are not sufficiently melted to become spheroidized and remain irregularly shaped. When the feed rate is decreased, the fraction of melted particle increases and eventually almost all particles become spherical. At the feed rate of 11 g/min, particle evaporation occurs, and spongy mass appears, as illustrated in Fig. 8(b). When the feed rate is further reduced to 6 g/min, a large amount of spongy mass is generated, as seen in Fig. 8(c).

The crystal phase of powder products also gives information about the melting and cooling histories of particles during their treatment in the plasma. Homogeneous nucleation in liquid droplets and solidification of alumina at considerable under cooling results in the formation of γ-alumina rather than α-alumina because of its lower critical free energy for homogeneous nucleation,[21] and α-phase alumina is formed in partially melted particles only by solidification onto non-melted seeds. Therefore, the volume fraction of the α-phase alumina, C_α, qualitatively indicates the fraction of non-melted part in the particles. Figure 9 illustrates the measured volume fraction of α-alumina after treatment in Ar–H_2 and Ar–N_2 plasmas under different particle feeding conditions. As expected, the fraction of solid or the non-melted fraction of powders increases with the powder feed rate. However, the volume fraction of α-phase in the Ar–N_2 plasma treated powders is less than that in the Ar–H_2 plasma treatment.

The α-phase formation in alumina can be attained through a moderated under cooling and nucleation history in melts, while γ-phase formation is preferred under considerable high under cooling.[21] Since the temperature of the Ar–H_2 plasma is obviously lower than that of the Ar–N_2 in the downstream regions, it would be expected that the cooling

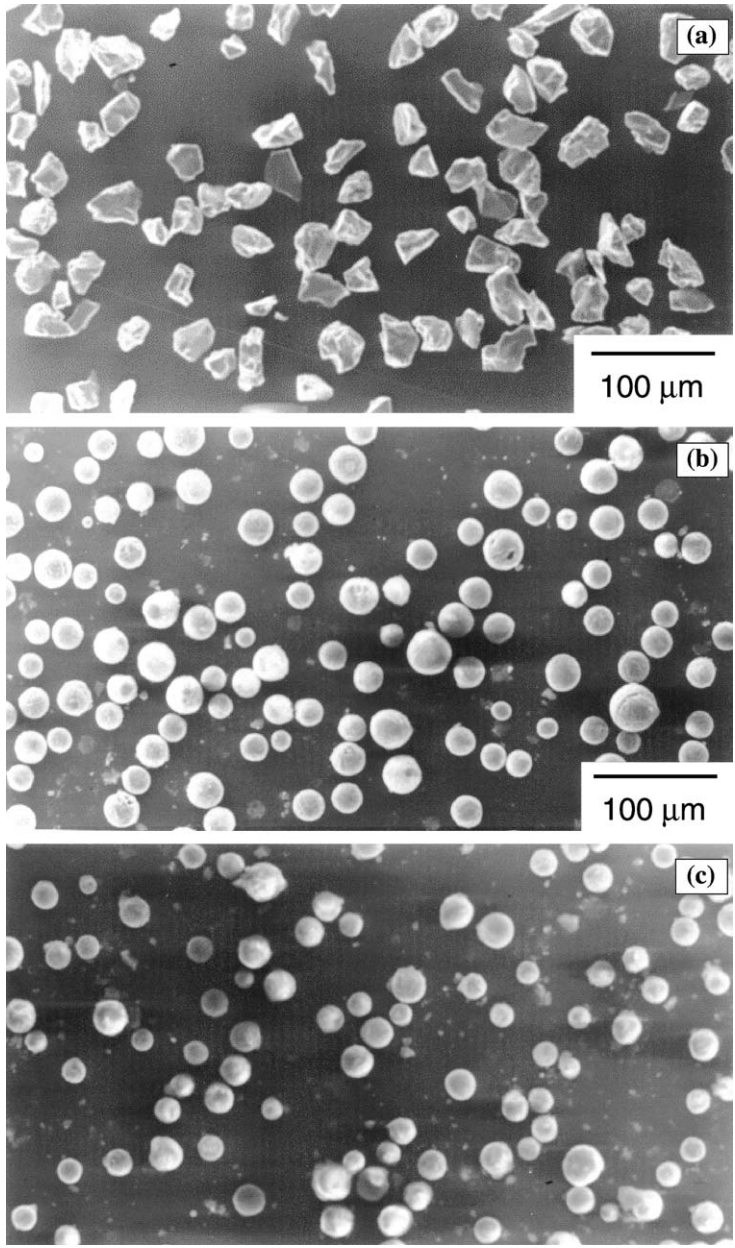

Fig. 7. SEM photographs of the Ar–N_2 plasma treated alumina powders. (a) Initial powders; (b) feed rate = 11 g/min; (c) feed rate = 2 g/min.

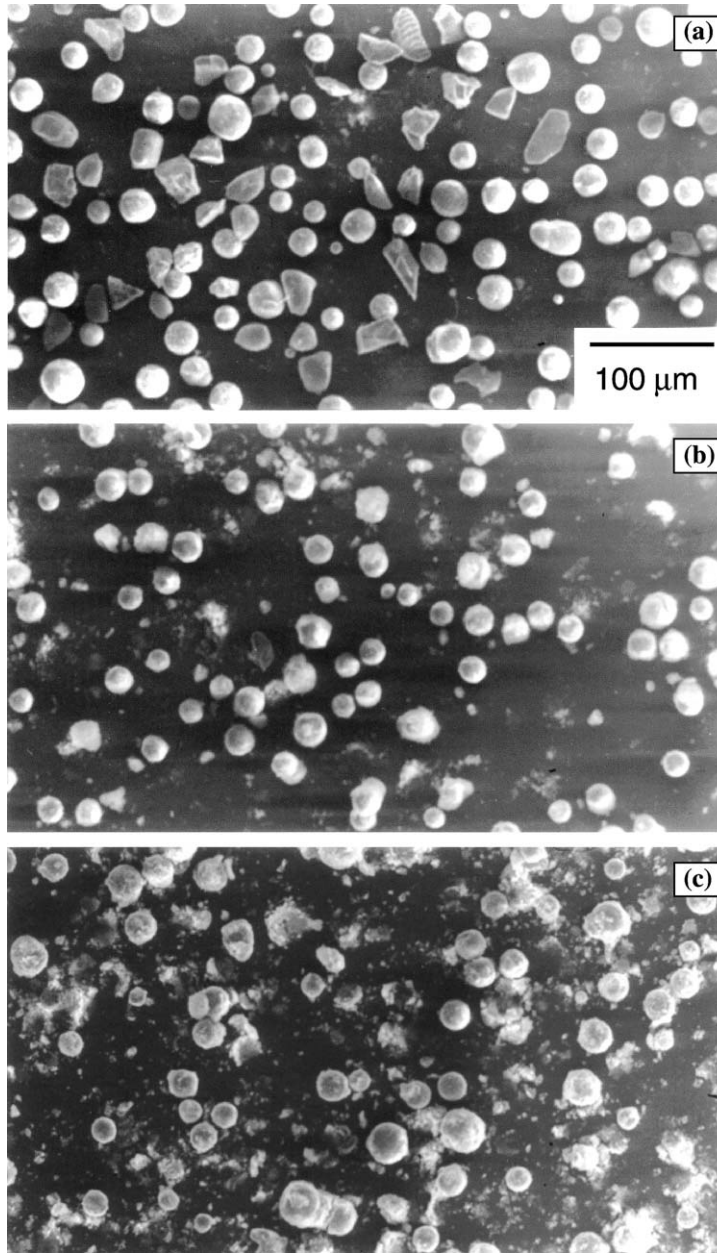

Fig. 8. SEM photographs of the Ar–H_2 plasma treated alumina powders. (a) Feed rate = 47 g/min; (b) feed rate = 11 g/min; (c) feed rate = 6 g/min.

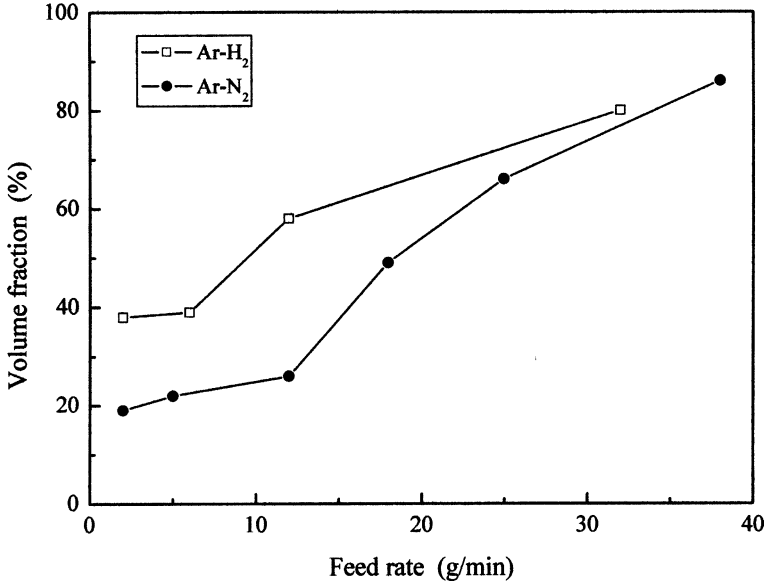

Fig. 9. The volume fraction of α-phase to the total amount of collected alumina powders.

rate of particles in Ar–H_2 plasma is higher. This would result in the production of γ-phase alumina. However, more evaporation takes place in the Ar–H_2 plasma, which will cool the gas surrounding the particles, decrease the temperature gradient close to the particles, and therefore, the cooling rate. The evaporated species coagulate to form a spongy mass surrounding the spheroidized particles. This explains the higher volume fraction of α-phase that is formed in the Ar–H_2 plasma compared to the Ar–N_2 plasma.

5. CONCLUSIONS

In this work, investigations on the RF plasma spheroidization of alumina powders involving particle heating and evaporation were carried out. Mathematical modeling results are compared with experimental data obtained under the corresponding operating conditions. Heating and evaporation of alumina particles in two different plasmas, Ar–H_2 and Ar–N_2, were studied to highlight the effects of plasma working gases on the plasma–particle heat transfer, which determines the particle size, shape and crystal phase of the products. The SEM photographs show that spheroidization of the alumina powder was achieved in both the Ar–H_2 and the Ar–N_2 RF plasmas, with the crystal phase varying

with the particle feed rate. The calculations predict that the plasma–particle heat transfer rate in the $Ar–H_2$ plasma is smaller than that in the $Ar–N_2$ plasma. The predicted particle size distributions for the $Ar–H_2$ and $Ar–N_2$ plasmas fit the measurement results well under high particle feed rate conditions. The overestimation of the plasma–particles heat transfer rate in the presence of particle evaporation suggests particle vapor plays an important role in the plasma–particle heat transfer. This effect should be included in modeling particle heating in thermal plasmas.

ACKNOWLEDGMENTS

The authors are very grateful to the financial support by the Consil de Recherche en Sciences Naturelles en Gènie de Canada (CRSNG) and the Fonds pour la Formation de Chercheurs et l'Aide a la Recherche (FCAR). Japan Society for the Promotion of Science and Technology Corporation is greatly acknowledged for providing a JSPS research fellowship to R. Ye.

REFERENCES

1. M. I. Boulos, *Pure Appl. Chem.* **68**, 1007 (1996).
2. M. I. Boulos, *High Temp. Mater. Process.* **1**, 17 (1997).
3. X. Fan, T. Ishigaki, and Y. Sato, *J. Mater. Res.* **12**, 1315 (1997).
4. T. Ishigaki and M. I. Boulos, *Ceram. Trans.* **22**, 139 (1991).
5. T. Ishigaki, Y. Bando, Y. Moriyoshi, and M. I. Boulos, *J. Mater. Sci.* **28**, 4223 (1993).
6. K. Chen, *Etude de procédés de déposition par plasma inductif*, PhD Thesis, University of Sherbrooke, Quebec, Canada, 1993.
7. C. T. Crowe, M. P. Sharma, and D. E. Stock, *J. Fluids Eng.* **99**, 325 (1977).
8. K. Chen and M. I. Boulos, *J. Phys. D: Appl. Phys.* **27**, 946 (1994).
9. E. Pfender and Y. C. Lee, *Plasma Chem. Plasma Process.* **5**, 211 (1985).
10. E. Pfender, *Plasma Chem. Plasma Process.* **9**, 167S (1990).
11. R. Ye, P. Proulx, and M. I. Boulos, *J. Phys. D: Appl. Phys.* **33**, 2154 (2000).
12. P. Proulx, J. Mostaghimi, and M. I. Boulos, *Int. J. Heat Mass Transfer* **28**, 1327 (1985).
13. S. V. Patankar, *Numerical Heat Transfer and Fluid Flow*, McGraw-Hill, New York, 1980.
14. M. I. Boulos, P. Fauchais, and E. Pfender, *Thermal Plasmas: Fundamentals and Applications*, Vol. 1, Plenum Press, New York, 1994.
15. R. B. Bird, W. E. Steward, and E. N. Lightfoot, *Transport Phenomena*, Wiley, New York, 1960.
16. S. L. Girshick and W. Yu, *Plasma Chem. Plasma Process.* **10**, 516 (1990).
17. X. Chen and E. Pfender, *Plasma Chem. Plasma Process.* **2**, 185 (1982).
18. M. Vardelle, C. Trassy, A. Vardelle, and P. Fauchais, *Plasma Chem. Plasma Process.* **11**, 185 (1991).
19. A. B. Murphy, *J. Phys. D: Appl. Phys.* **34**, R151 (2001).
20. A. B. Murphy, *Phys. Rev. E.* **55**, 7473 (1997).
21. R. McPherson, *J. Mater. Sci.* **8**, 851 (1973).